PAPER

Check for updates

Water droplet attraction and coalescence on liquid-crystal-infused textured and porous surfaces

Filip Ferš,[a] Xiaoguang Wang (ID)[bc] and Uroš Tkalec (ID) *[ade]

Coalescence of droplets on liquid-infused surfaces has been extensively investigated for isotropic lubricants, where interfacial and hydrodynamic responses are well described by geometry-based and mass-spring models. However, the corresponding dynamics on anisotropic lubricating films, such as liquid crystals (LCs), remain largely unexplored. In this work, we report the use of high-speed imaging to study the attraction and coalescence of millimetre-sized water droplets on two classes of substrates, covered with a thin LC overlayer: LC-infused textured surfaces (LCITS) and LC-infused porous surfaces (LCIPS). On both substrates, the droplets coalesce in three stages over approximately one minute: long-range capillary-mediated attraction, drainage of the lubricant within the wetting ridge, and final merging accompanied by in-plane oscillations of the formed droplet. On LCITS, the initial approach velocities and post-merging dynamics are broadly consistent with the geometry-based mass–spring model developed for oil-impregnated surfaces of a similar type. However, on LCIPS, where a thicker lubricating film produces a larger wetting ridge, we observe substantially reduced attraction and merging velocities, no oscillations were resolved within our temporal resolution at the first velocity peak, and drainage times strongly influenced by evaporation. In the final stage, the peak velocity mainly depends on the LC mesophase and is nearly independent of droplet size, while the oscillation period scales approximately with the square root of the droplet radius. These results clarify how the porous LC scaffold and enlarged wetting ridge alter droplet–droplet interactions and coalescence dynamics relative to textured silicone substrates.

1 Introduction

The need for liquid repellency to prevent biofouling,[1–3] reduce icing,[4] and permit self-cleaning[5] has driven the development of robust liquid-repellent surfaces. One successful approach infuses textured or nanoporous substrates with a chemically compatible lubricant that repels immiscible liquids, forming slippery liquid-infused porous surfaces (SLIPS).[6–8] The intercalated lubricant film is smooth, defect-free, and self-healing, which greatly suppresses contact-line pinning and allows droplets to slide or roll off at very small tilt angles.[8–11] The performance of SLIPS depends sensitively on the chemical

compatibility between the lubricant, working fluid, and substrate, and can be compromised by contamination, phase separation, or lubricant loss.[6,10] In particular, droplets siphon the lubricant into a wetting ridge around their base, progressively depleting the infused layer and modifying droplet mobility over time.[11–15]

Conventional SLIPS are typically infused with inert isotropic oils whose interfacial and rheological properties are essentially static.[6,7,16] While careful structuring of the substrate can provide some degree of passive control,[17–20] such surfaces offer limited real-time tunability. To address this, recent work has replaced passive oils with functional lubricants, including thermotropic liquid crystals (LCs), whose elasticity, interfacial tensions, and rheological properties can be tuned by temperature, light, and electric or magnetic fields.[21–25] LC-infused surfaces thus represent a new class of adaptive, multifunctional slippery materials with potential for next-generation open-surface microfluidics, droplet-based transport, and sensing.[26–30]

In this work, we distinguish between two classes of LC-infused surfaces. LC-infused textured surfaces (LCITS) are formed by infiltrating textured substrates, such as silicone

[a] *Institute of Biophysics, Faculty of Medicine, University of Ljubljana, 1000 Ljubljana, Slovenia. E-mail: uros.tkalec@mf.uni-lj.si*

[b] *William G. Lowrie Department of Chemical and Biomolecular Engineering, The Ohio State University, Columbus, OH 43210, USA*

[c] *Sustainability Institute, The Ohio State University, Columbus, OH 43210, USA*

[d] *Faculty of Natural Sciences and Mathematics, University of Maribor, 2000 Maribor, Slovenia*

[e] *Department of Condensed Matter Physics, Jožef Stefan Institute, 1000 Ljubljana, Slovenia*

micropillars or PTFE membranes, with a thermotropic LC.[6,30,31] In contrast, LC-infused porous surfaces (LCIPS) consist of a nanoporous crosslinked LC network swollen with a low-molar-mass LC.[25–27,32] In both cases, a lubricant film separates droplets from the underlying solid, achieving nearly hysteresis-free motion.[8,10,33] The droplets siphon the lubricant from the surrounding film into an annular wetting ridge around their base,[14,34] which mediates long-range capillary interactions,[13,35–37] serves as a primary site of viscous dissipation during motion,[9,38–40] and is a dominant pathway for lubricant loss.[11,12,15,41] When the spreading coefficient of the lubricant on the droplet is positive, droplets can also become cloaked by a thin lubricant film, providing an additional, though typically smaller, contribution to lubricant depletion.[34] On soft solid substrates, related wetting ridges can even hinder coalescence and lead to a "reluctance to coalesce", underscoring the key role of deformable interfaces in droplet interactions.[42]

The classic coalescence of droplets without an infused lubricant is governed by rapid neck growth, controlled by a balance of capillary, viscous, and inertial forces.[43,44] In this case, coalescence occurs on millisecond time scales and is well described by similarity solutions for the neck radius as a function of time. In contrast, on oil-based SLIPS, droplet attraction and coalescence proceed through three distinct stages: (i) capillary-force-mediated attraction as wetting ridges overlap, (ii) drainage of the lubricant film trapped between the droplets, and (iii) merging accompanied by pronounced shape deformations and in-plane oscillations of the merged droplet.[10,15,36] These dynamics are quantitatively captured by a geometry-based model coupled to a classical mass–spring description, in which the effective interfacial tension and lubricant viscosity set the characteristic velocities, time scales, and energy partitioning.[36,37] However, this framework has so far been developed and validated only for isotropic lubricants. Whether it applies to LC-infused systems – and how LC anisotropy, mesophase, and wetting-ridge morphology modify coalescence dynamics – remains unknown.

Here, we experimentally investigate water droplet attraction and coalescence on LCITS and LCIPS, and compare our results with the theoretical framework of Xu et al.,[36] originally developed for oil-infused SLIPS. While both lubricant- and LC-infused surfaces rely on a locked lubricant layer to minimize contact line pinning, the anisotropy and phase-dependent behaviour of LCs enable active control of droplet mobility and interfacial interactions via external stimuli such as temperature, light, or magnetic field.[26,27] Although surfaces infused with isotropic lubricants exhibit excellent slipperiness, control remains largely passive, limited to fixed parameters such as lubricant viscosity, surface chemistry, and static patterning rather than reversible, field-driven tuning.[16,45] We study LCIPS and LCITS because they are both similar to more traditional SLIPS, yet rely on distinct substrate architectures to immobilize the lubricant, namely microstructured pillar arrays versus nanoporous networks.[6,9,39] Microstructured surfaces confine the lubricant primarily at the surface between discrete features, which has been

shown to promote prominent wetting ridge formation, and to localize viscous dissipation in the wetting ridge.[9,39,46] In contrast, nanoporous networks retain the lubricant volumetrically, leading to enhanced lubricant stability and sustained lubrication even under repeated droplet motion or deformation.[6,45] Prior studies demonstrate that these differences influence droplet mobility, dissipation, and stability of the lubricating layer, motivating a comparison of droplet coalescence across both substrate classes using LCs as a lubricant.[6,9,39,45] Using high-speed imaging, we resolve the three stages of coalescence on both types of substrate and quantify how the LC phase and wetting ridge height affect approach velocities, drainage times, and post-merging oscillations. By combining these measurements with LC-specific material parameters, we assess the extent to which the geometry-based mass–spring model can be applied to anisotropic lubricants and identify regimes where LC-specific effects and large wetting ridges cause systematic deviations. These insights provide guidelines for designing LC-based SLIPS with controllable droplet interactions for open-surface microfluidics and related applications.

2 Experimental details

2.1 Materials

We used the thermotropic LC 4-cyano-4′-pentylbiphenyl (5CB, Synthon Chemicals), which exhibits a nematic phase between 22.5 °C and 35 °C, to prepare thin liquid films on LCITS by spin-coating. The other LC, 4′-octyl-4-biphenylcarbonitrile (8CB, Synthon Chemicals), which shows a smectic A phase at room temperature and a nematic phase between 33.5 °C and 40.2 °C,[47] was used only in combination with LCIPS. As the smectic A phase significantly increases droplet sliding angles on LCIPS due to its layered structure,[27] we limited our experiments to the nematic and isotropic phases of both LCs. Their physical properties in the selected mesophases, such as density and viscosity (η_{LC}),[48–50] are similar for 5CB and 8CB, and these materials have already been used in previous LCIPS studies, together with the commercial LC mixture E7.[25–28,30,32] Temperature-dependent surface tension in air (γ_{LC})[27,51] and interfacial tension with water ($\gamma_{LC,w}$)[25,27,52,53] are summarized in Table 1. For the viscosity, we selected the second Miesowicz coefficient $\eta_2 \approx 0.02$ Pas, which corresponds to shear flow with the nematic director aligned parallel to the flow direction[54] (see Table S1). This configuration was assumed for our system, although it was not explicitly measured.

Table 1 Surface tension of LCs in contact with air (γ_{LC}) and interfacial tension between the LCs and water ($\gamma_{LC,w}$) in the nematic and isotropic phases at the indicated temperatures T. The values for 8CB are close to those recently measured by Xu et al.[32]

LC	Phase	T [°C]	γ_{LC} [mN m^{-1}]	$\gamma_{LC,w}$ [mN m^{-1}]
5CB	Nematic	30	25.3	31.2
5CB	Isotropic	40	45.0	29.7
8CB	Nematic	40	23.6	17.6
8CB	Isotropic	50	31.4	13.5

For the preparation of LCIPS, the following chemicals were purchased from Sigma-Aldrich: photoinitiator 2,2-dimethoxy-2-phenylacetophenone (DMPAP), silane dimethyloctadecyl(3-(trimethoxysilyl)propyl)ammonium chloride (DMOAP, 60% in methanol), and reactive LC monomer 1,4-bis-(4-(3-acryloyl-oxypropyloxy)benzoyloxy)-2-methylbenzene (RM257). Silicon wafers were obtained from Nova Electronic Materials, and the micropillar array was fabricated by coating a wafer with a photoresist, followed by UV exposure using a Karl Suss MJB-3 contact aligner to define the desired pattern. The textured photoresist then served as an etch mask for sculpting the wafer surface using an ETC01 Technics reactive ion etching system.[30] The photoresist was removed by oxygen plasma exposure. Plain microscope slides were obtained from the Karl Hecht glassware factory, and deionized water was purchased from Mikro + Polo. All chemicals were used as received.

2.2 Preparation of LCITS and LCIPS

The textured silicon substrate was plasma treated for 2 min (Expanded Plasma Cleaner PDC-002, Harrick Plasma) and functionalized by immersing the substrate in a 2 wt% DMOAP solution in deionized water for 20 min. The substrate was then rinsed with isopropyl alcohol and deionized water to remove unreacted DMOAP, and finally dried under a nitrogen stream. To obtain LCITS, approximately 300 μL of 5CB was heated to 50 °C and deposited on the substrate by spin-coating (WS-650-Mz-23NPP, Laurell) at 500 rpm for 60 s using a gradual acceleration profile. This produced a uniform ≈20 μm thick LC layer, covering micropillars with a height of 17 ± 0.5 μm, as measured by white light interferometry (see SI for details). The substrate was periodically cleaned and reinfused with fresh 5CB to ensure reproducibility across multiple measurements.

LCIPS were prepared following established protocols.[25,32] A mixture containing 90 wt% of the non-reactive mesogen 8CB, 10 wt% of the reactive monomer RM257, and 1 wt% of the photoinitiator DMPAP was prepared. The mixture was heated to 100 °C and vortexed until homogeneous. Approximately 100 μm of the mixture was deposited between two glass slides separated by 100 μm spacers. The top slide was functionalized with a 2 wt% DMOAP solution in deionized water for 20 min to ensure strong homeotropic surface anchoring. After the deposited mixture cooled to the nematic phase, the samples were illuminated with UV light of 365 nm to polymerize RM257, resulting in a nanoporous poly(RM257) network swollen with 8CB. The slides were then separated and the residual LC was removed by rinsing the surface with isopropyl alcohol and deionized water, followed by drying with a nitrogen stream. To form the lubricating film, pure 8CB was drop-cast onto the surface in an amount corresponding to a ~100 μm thick layer. The amount deposited was verified by weighing the surface on an analytical balance (ABJ 320-4NM, Kern) before and after drop-casting to ensure a consistent LC film thickness between measurements. Schematics showing a water droplet residing on LCITS and LCIPS are presented in Fig. 1.

2.3 Droplet generation and micromanipulation

LCIPS and LCITS samples were heated on a thermo plate stage (Tokai Hit), as shown in Fig. 2a. For 5CB, the temperature set
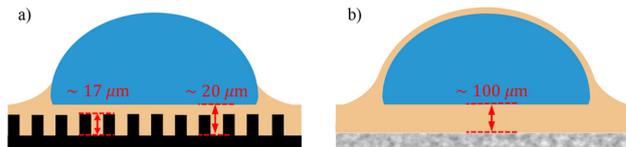

Fig. 1 Schematics showing water droplets on (a) LCITS infused with 5CB, where the droplet may not be fully encapsulated by the LC. The lubricating film has a thickness of approximately 20 μm, including the pillar height of 17 μm; (b) LCIPS infused with 8CB, where the droplet is fully encapsulated by the LC and rests on an approximately 100 μm thick lubricating layer of LC.
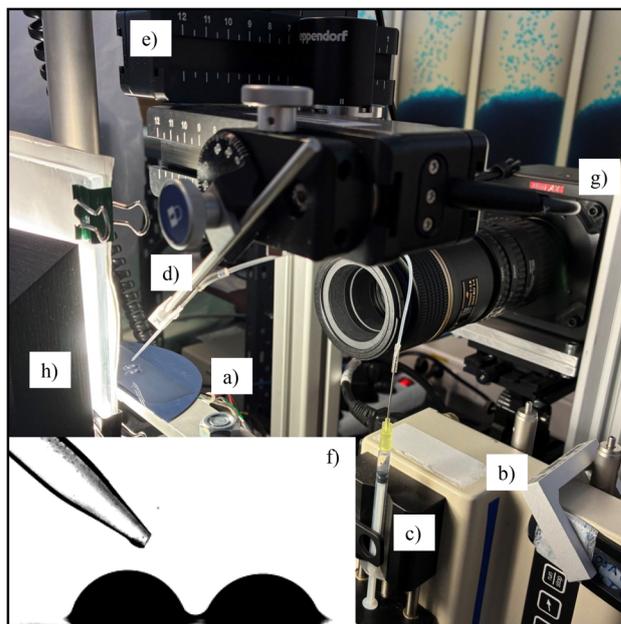

Fig. 2 Experimental setup for droplet coalescence measurements. Two droplets are deposited on a LCITS sample mounted on a thermo plate stage (a). Droplets are generated using a syringe pump with adjustable flow rate (b) and a mounted syringe (c), and deposited via a glass capillary (d) attached to a capillary holder on a micromanipulator (e). A high-speed camera (g) and a backlighting system (h) provide high-contrast imaging of droplet attraction and coalescence. Inset (f) shows two droplets and the capillary tip during droplet deposition.

points were 30 °C and 40 °C, while for 8CB they were 40 °C and 50 °C. Direct measurements of the metal plate surface with a K-type thermocouple showed that the surface temperature was approximately 2 °C below the set point; throughout this work, we report the nominal set point temperatures.

Droplets were generated using a syringe pump (KDS 100, Fisher Scientific) operated at a flow rate of 0.5 mL h^{-1} (Fig. 2b), producing droplet volumes in the range of 0.7 μL to 3.5 μL (radii 0.3 mm to 1.2 mm), determined by the generation time. A 1 mL syringe (Troge Medical; Fig. 2c) was connected to a glass capillary treated with DMOAP and positioned at the same height as the LC surface to minimize hydrostatic pressure differences and reduce adhesion at the tip of the capillary, thereby facilitating droplet detachment (Fig. 2d). The capillary was mounted on a micromanipulator (InjectMan4, Eppendorf),

which was used to deposit droplets and to translate them at the LC surface (Fig. 2e).

The droplets were initially placed on the heated surface at a distance greater than the interaction range. One droplet was then moved towards the other using the micromanipulator arm. Once the wetting ridges overlapped, the capillary was retracted (Fig. 2f). This procedure ensured that the interaction between droplets was initiated almost entirely through capillary-mediated attraction.

2.4 High-speed imaging and image analysis

The dynamics of the droplets were recorded using a high-speed camera (FASTCAM Mini AX200, Photron) operating at 10 000 fps (Fig. 2g). High-resolution imaging of millimetre-sized droplets was achieved with a macro lens (SP AF 90 mm f/2.8 Di, Tamron) combined with three extension tubes. The droplet stage was backlit with two air-cooled LED lights (XLamp-CMA2550, Cree) to provide high contrast and clear visualization of the droplet silhouettes (Fig. 2h).

The captured image sequences were analyzed using custom scripts in Python (Python Software Foundation). Prior to analysis, standard preprocessing was applied, including background subtraction, contrast enhancement, Gaussian blurring, and intensity thresholding. In the first stage of coalescence, both droplet outlines were fitted with circles using a circular Hough transform. The distance between the centers of the fitted circles ($2l$) was taken as the distance between the centers of mass of the droplets and tracked over time (Fig. 3a). The instantaneous approach velocity u was then calculated as $u = -dl/dt$ (Fig. 3d).

In the second stage, the time delay associated with lubricant drainage was measured manually, starting from the first velocity peak (just before the droplets collide) and ending when the droplets merge. The uncertainty of these manually determined times is on the order of a few seconds. In the third stage, droplet deformation prevented reliable circle fitting. Instead, instantaneous velocity (Fig. 3c and d) was approximated from the change in the total cross-sectional area of the droplets S as $u = -1/(2h)dS/dt$, where the height of the meniscus h (Fig. 3a) converts the cross-sectional area into an effective length scale, and the factor 1/2 accounts for both droplets.

3 Summary of the theoretical model

To evaluate our experimental results, we used the theoretical framework developed by Xu *et al.*[36] This model describes droplet coalescence on oil-infused SLIPS using a geometry-based approach coupled with a classical mass–spring model. Coalescence is divided into three stages: capillary-force-mediated attraction as wetting ridges overlap (stage I), drainage of the trapped lubricant film (stage II), and merging accompanied by in-plane oscillations (stage III).

Initially, a millimetre-sized droplet with radius R (Fig. 3a), placed on a liquid-infused surface, draws the surrounding lubricant into an annular wetting ridge around its base (orange

arrow, Fig. 3b) due to an imbalance of interfacial forces along the three-phase contact line. Additionally, droplets may be enveloped by a thin wrapping layer whenever the spreading coefficient of the lubricant on water ($\psi_{l,w} > 0$) is positive.[34] In this case, the cloaked droplet has two interfaces, the lubricant–air (γ_l) and the lubricant–water ($\gamma_{l,w}$) interfaces (Fig. 3b), which are accounted for by an effective interfacial tension $\gamma_{eff} = \gamma_l + \gamma_{l,w}$. The wetting ridge and the morphology of millimetre-sized droplets are fully determined by interfacial forces, since the capillary length L_c is much greater than the droplet radius ($L_c \gg R$).

In stage I, coalescence is initiated when the wetting ridges of two neighbouring droplets overlap, generating a capillary interaction that drives the droplets towards each other. A simple geometric model of two approximately hemispherical droplets whose centres of mass are separated by a distance $2l$ shows that the horizontal approach velocity of the droplets is approximately equal in magnitude to the vertical rise velocity of the lubricant on the wetting ridge:

$$\left|\frac{dl}{dt}\right| \approx \left|\frac{dh}{dt}\right|. \tag{1}$$

The peak approach and meniscus rise velocities, $u_1 \approx (dl/dt)_{max}$ and $u_h = (dh/dt)_{max}$, are therefore also approximately equal. This relationship has been verified across a range of droplet sizes, lubricant viscosities, and textured substrate geometries.[36] By balancing the attractive capillary force acting on each droplet, $F_\gamma \sim R\gamma_l$, with the viscous force

$$F_\eta \approx 2.6(2\pi)\gamma_{l,w}R\left(\frac{u_1\eta_l}{\gamma_{l,w}}\right)^{2/3},$$

where η_l is the lubricant viscosity, the first peak velocity can be approximated as

$$u_1 \approx \left(\frac{\gamma_l}{5.2\pi\gamma_{l,w}}\right)^{3/2}\frac{\gamma_{l,w}}{\eta_l}. \tag{2}$$

In stage I, the droplets oscillate in their position l and in the approach velocity $-dl/dt$, with a characteristic oscillation period

$$\tau_1 \sim \left(\frac{\rho R^3}{\gamma_{eff}}\right)^{1/2}, \tag{3}$$

where ρ is the density of water.

In stage II, the droplets collide, leaving a thin lubricant film of thickness b trapped between them (Fig. 3b). This nearly flat film, whose geometry can be approximated by a semicircle with radius $h \approx R$, prevents the droplets from merging immediately. The trapped lubricant is drained by the pressure difference between the flat film region and the surrounding meniscus, which can be approximated by a circular arc with radius r_h (Fig. 3b). The resulting pressure difference Δp is

$$\Delta p = \frac{2(\gamma_l + \gamma_{l,w})}{R} - \frac{\gamma_l}{h} + \frac{\gamma_l}{r_h}. \tag{4}$$
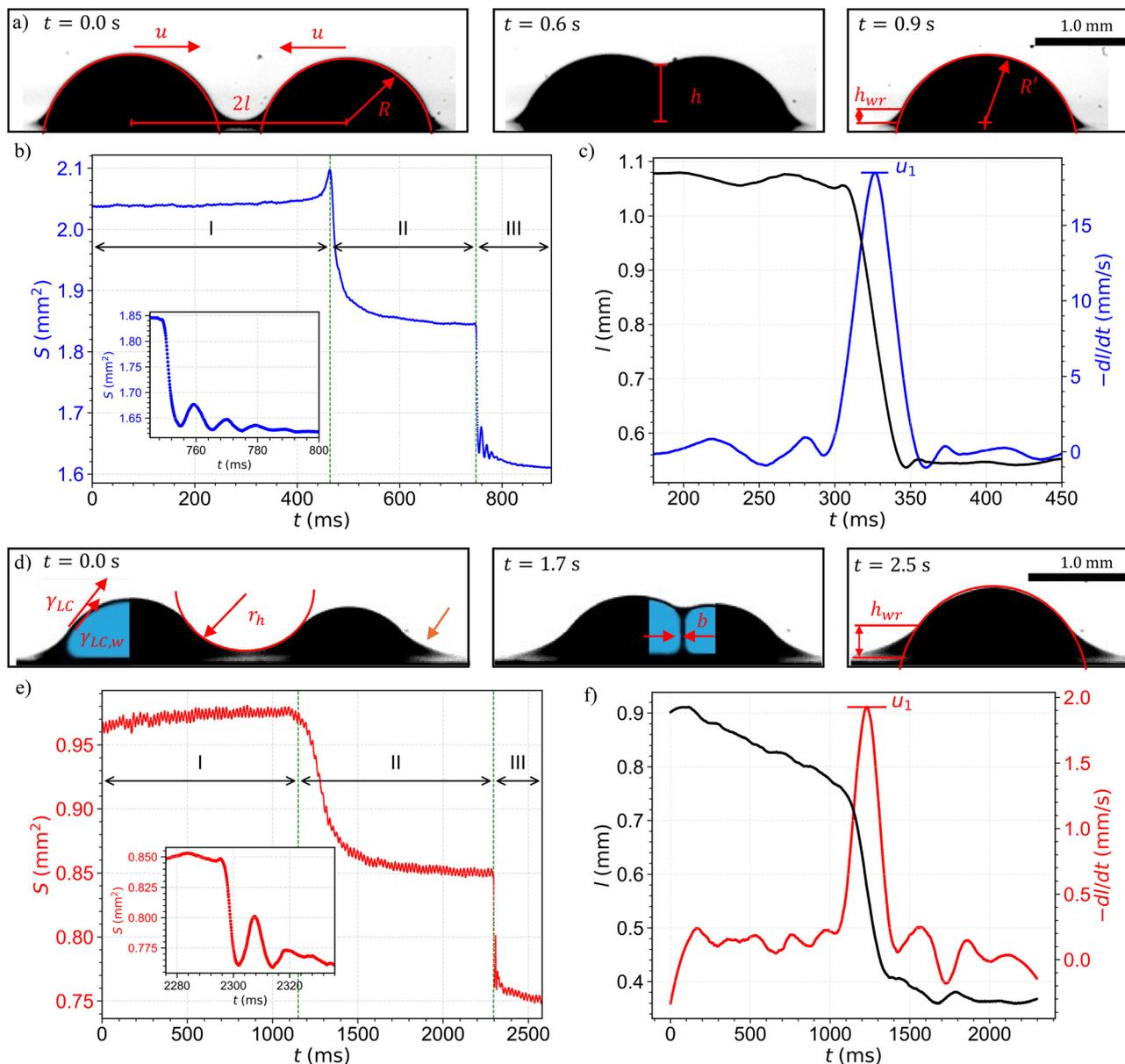
Fig. 3 Time-lapse sequence of droplet coalescence on (a) LCITS and (d) LCIPS. The two droplets, approximated as hemispheres with initial radius R, approach each other with velocity $-dl/dt$. As they approach, the distance between droplets $2l$ decreases and the meniscus height h increases at approximately the same rate. The meniscus, which can be approximated as an arc with radius r_h, also decreases as the droplets approach each other. The droplets become encapsulated by a thin LC film, giving rise to two interfacial tensions, at the LC−air interface (γ_{LC}) and at the LC−water interface ($\gamma_{LC,w}$). A thin LC film of thickness b separates the droplets, preventing immediate merging into a single larger droplet of radius R'. On LCIPS, the wetting ridge h_{wr} is larger than on LCITS (orange arrow). Time evolution of the total cross-sectional area of the two droplets S over all three stages of coalescence on (b) LCITS and (e) LCIPS. The inset highlights oscillations in S during droplet merging in the third stage. Time evolution of the droplet position l (left axis), and approach velocity $-dl/dt$ (right axis), is shown for (c) LCITS and (f) LCIPS, including peak velocity u_1. No oscillations were resolved within our temporal resolution in droplet position at the first velocity peak on either surface.

Using the lubrication approximation with a Poiseuille flow model in a transition region of size $(br_h)^{1/2}$ yields the drainage time Δt:

$$\Delta t \approx \frac{\eta_l h r_h^{1/2}}{\Delta p b_f^{3/2}}, \tag{5}$$

where b_f is the final film thickness, on the order of 100 nm.

Experimentally, the drainage time appears as the time lag between the peaks of velocity and acceleration.

In stage III, after the thin film ruptures, two droplets of radius R merge to form a single droplet with a larger radius $R'=2^{1/3}R$, reducing the interfacial area from $4\pi R^2$ to $2^{5/3}\pi R^2$. This reduction releases surface free energy, part of which is converted into the translational kinetic energy of the merged droplet. The released energy causes significant droplet

deformation and induces in-plane oscillations in the horizontal direction. The second peak velocity u_2 can be estimated from a simple energy balance as

$$u_2 \approx 1.1 \left(\frac{\gamma_{\text{eff}}}{\rho R} \right)^{1/2}. \tag{6}$$

The release of surface free energy and the subsequent oscillations in S and $-\,\mathrm{d}S/\mathrm{d}t$ are well described by a damped harmonic oscillator. In this framework, the effective interfacial tension γ_{eff} acts as a restoring force analogous to a spring, while the lubricant viscosity η_l damps the motion of droplets with mass $\sim \rho R^3$. This model explains not only the period of oscillation at the second peak,

$$\tau_2 \approx \left(\frac{\rho R^3}{\gamma_{\text{eff}}} \right)^{1/2}, \tag{7}$$

but also the characteristic decay time ($t_{\text{decay}} \propto \eta_l^{-1}$), which determines the exponential damping of the oscillations in S and $-\mathrm{d}S/\mathrm{d}t$. Both relationships agree reasonably well with experiments.[36]

In this work, we apply the same model and associated scaling laws to evaluate droplet coalescence on LCITS and LCIPS. While we do not modify the theoretical equations, we use material-specific parameters, namely the interfacial tension, density, and viscosity of 5CB and 8CB in their respective mesophases. A complete derivation of the model is provided in Xu et al.[36] and the associated supplementary information.

4 Results and discussion

Before comparing our measurements with the theoretical model of Xu et al.,[36] we briefly clarify the notation used for the LC systems. In that model, the lubricant is treated as an isotropic liquid characterized by surface tension γ_l, lubricant–water interfacial tension $\gamma_{l,w}$, and viscosity η_l. In our experiments, the lubricant is 5CB or 8CB in either the nematic or isotropic phase, so γ_l and $\gamma_{l,w}$ correspond to the phase-dependent LC–air and LC–water interfacial tensions γ_{LC} and $\gamma_{\text{LC,w}}$ (see Table 1). The effective interfacial tension in the model is therefore $\gamma_{\text{eff}} = \gamma_{\text{LC}} + \gamma_{\text{LC,w}}$ in the corresponding mesophase. The viscosity of LCs depends on the orientation of the nematic director relative to the flow fields, while the flow field can reorient the director. As a result, the appropriate viscosity must be selected based on the director configuration and shear geometry relevant to the mesophase and each stage of droplet coalescence. Previous studies of LC-infused surfaces show that viscous dissipation is dominated by flow within the wetting ridge.[9,39] We assume the energetically favored configuration in which the nematic director is predominantly aligned parallel to the local flow direction. This configuration corresponds to the lowest of the three Miesowicz viscosities, the second Miesowicz coefficient η_2, which we take as the apparent viscosity η_l; these anisotropic viscosity coefficients are defined only in the nematic phase where a director exists,[50] whereas in the isotropic phase, orientational order is lost and the Miesowicz

viscosities collapse to a single isotropic shear viscosity ($\eta_1 = \eta_2 = \eta_3$), which we use as the apparent viscosity in the isotropic phase.

Our choice is supported by prior studies with 5CB and 8CB, which show that flow-aligned configurations exhibit nearly Newtonian behavior with weak shear-rate dependence, whereas director rotation, twist or shear-induced reorientation leads to higher viscosities and shear-thinning behavior.[55] Independent droplet breakup experiments further indicate that both 5CB and 8CB behave effectively as Newtonian fluids in the nematic phase, with viscosities of 20 to 30 mPa s, consistent with η_2 dominated flow rather than higher Miesowicz coefficients.[56] The apparent viscosities previously measured on LC-infused surfaces fall close to the lowest Miesowicz viscosity, in the range of 20 to 38 mPa s,[27,32] further supporting our selection. Assuming that 5CB behaves as 8CB under comparable anchoring and shear conditions, we use η_2 for both materials in the nematic phase. During the second stage of coalescence, the LC is confined to a film of thickness ~ 100 nm with degenerate planar anchoring at the LC–water interface.[32] In this geometry, the director lies predominantly parallel to the film plane. For pressure-driven (Poiseuille-like) flow in confined films[36] in the nematic phase, the apparent viscosity is close to the flow-aligned value η_2. During the third stage, flow is minimal. Consistent with this, the peak velocity u_2 is independent of viscosity, indicating that viscous dissipation is not dominant in this regime. In general, this treatment neglects possible transient director distortions during rapid flow. However, given the observed agreement between previously measured apparent viscosities and rheological data, we believe that the use of η_2 provides a reasonable and physically motivated approximation for the apparent viscosity in the nematic phase governing dissipation in our system.

After infusing the LCITS and LCIPS with their constituent LCs, deionized water droplets were deposited onto the surface using a micromanipulator (Fig. 2e). Because no surfactants or electrolytes were added to the water droplets, interfacial effects are governed primarily by LC anchoring and wetting. Cyanobiphenyl LCs anchor homeotropically at the air–LC interface and degenerate planar at the water–LC interface, so water droplets induce LC reorientation and elastic distortions near the interface.[32] Absorption-driven charging is therefore minimized and electrostatic effects from trace ions in deionized water are not expected to dominate the observed coalescence behavior. At the three-phase contact line, the three interfacial tensions satisfy a vectorial force balance at the contact line $\gamma_{\text{LC}} + \gamma_{\text{LC,w}} + \gamma_{\text{w}} = 0$, where γ_{w} is the surface tension of water. This force balance creates a concave meniscus with a negative pressure relative to the ambient pressure, which draws the LC inward into an annular wetting ridge, as is characteristic for droplets on liquid-infused surfaces.[57] While interfacial tensions govern ridge formation and constrain the admissible geometry, they do not set the numerical prefactor of the normalized steady-state height. Previous studies have shown that for thin lubricant layers, the wetting ridge height depends on the available lubricant thickness. Above a critical thickness, the system

enters an excess-lubricant regime in which the wetting ridge geometry becomes insensitive to further increases in lubricant layer thickness, whereas for thinner layers the ridge remains supply-limited.[14] When sufficient lubricant is available to reach the excess lubrication regime and the Neumann condition is satisfied, the wetting ridge grows to its steady-state height of $h_{wr}/R_d \approx 0.6$ on oil-infused surfaces,[14,57] as also observed here for LC surfaces. For our droplets, the wetting ridge morphology is therefore governed primarily by capillary forces at the water–LC interface, because $R \ll L_c$. The capillary length of a fluid interface is defined as

$$L_c = \left(\frac{\gamma_{LC,w}}{\Delta \rho g}\right)^{1/2}, \quad (8)$$

where $\Delta \rho = |\rho_w - \rho_{LC}|$ is the density difference between the fluids (values from Table S1) and g is the gravitational acceleration. Using literature values[25,27,48,49,51–53,58] for $\gamma_{LC,w}$ (Table 1), densities and viscosities (Table S1), we obtain capillary lengths (L_c) of ≈ 9 mm and 12 mm for 8CB at 40 °C and 50 °C, respectively, and ≈ 13 mm and 15 mm for 5CB at 30 °C and 40 °C, respectively. As all droplet radii used in this study (0.3 mm to 1.2 mm) are well below these values, gravitational effects are negligible. Under these conditions, previous work has shown that the steady-state wetting ridge height on oil-infused surfaces scales primarily with droplet size for hemispherical droplets at low Bond number, approaching $h_{wr} \approx 0.56R$.[57] The Bond number is defined as

$$Bo = \frac{\Delta \rho g R^2}{\gamma_{LC,w}}, \quad (9)$$

where the characteristic length was taken as the droplet radius. Using an average droplet radius of $R = 0.6$ mm, we obtain Bond numbers $Bo \approx 2.1 \times 10^{-3}$ and 1.6×10^{-3} for 5CB in the nematic and isotropic phases, respectively, and 2.6×10^{-3} and 4.7×10^{-3} for 8CB in the nematic and isotropic phases, respectively. Since these values are well below the validity limit of the geometry-based model (Bo < 0.25), we expect the steady-state wetting ridge height in our experiments to approach the theoretical value $h_{wr} \approx 0.56R$, provided sufficient lubricant is available. As described in Section 2, the thickness of the LC layer on LCITS is ≈ 3 μm above the micropillar array, as confirmed by white light interferometry (micropillar height is 17 ± 0.5 μm), and the thickness of the LC layer on LCIPS is ≈ 100 μm as measured gravimetrically. By treating our nanoporous LCIPS as effectively planar and operating in the excess-lubrication regime, the wetting ridge is insensitive to changes in film thickness and will grow to its steady-state size.[14,57] Consistent with this, on LCIPS we measured a wetting ridge height $h_{wr} = 0.6 \pm 0.1R$, in good agreement with the theoretical 0.56R. On LCITS, it has been shown that overfilling the micropillar array strongly modulates the wetting ridge height.[12] On our LCITS samples, with only approximately 3 μm of lubricant above the micropillar array, we observed a smaller wetting ridge, $h_{wr} = 0.24 \pm 0.08R$. Thus, the overall difference in wetting ridge height between LCITS and LCIPS is consistent

with the fact that the availability of lubricant is the primary factor controlling h_{wr}, given that gravitational effects can be neglected, and provides a natural geometric control parameter for the subsequent dynamics of coalescence.

Tress et al.[14] showed that the wetting ridge has no intrinsic horizontal length scale; in the excess lubrication regime, the meniscus exhibits a logarithmic decay regularized only by the capillary length, whereas in the starved lubrication regime it is truncated by disjoining pressure and its extent is governed by the lubricant film thickness and molecular interactions rather than droplet size. Consequently, in the starved regime, an apparent radius r^* can be defined at which the meniscus height becomes negligible, rendering the wetting ridge height finite and well defined. In the excess lubrication regime, however, the meniscus extends over distances comparable to the lubricant capillary length and there is no well-defined outer radius; the ridge therefore lacks a sharp cutoff. On our surfaces in the starved lubrication regime (i.e., LCITS), the meniscus is localized and its horizontal extent is characterized by a finite apparent radius. By contrast, on LCIPS, which is in the excess lubrication regime, there is no obvious cutoff and the wetting ridge decays over a length scale comparable to the lubricant capillary length $L_C = (\gamma_{LC}/\rho_{LC}g)^{1/2}$. For LCIPS, we obtain $L_{C,8CB} \approx 5.5$ mm in the nematic phase and $L_{C,8CB} \approx 6.3$ mm in the isotropic phase. Accordingly, wetting ridges on LCITS have a clear and sharp cutoff, whereas on LCIPS it is ambiguous where the wetting ridge flattens out. Approximate measurements of the wetting ridge length L yield, on LCIPS, $L = 1.4 \pm 1.0$ mm in the nematic phase and $L = 1.9 \pm 1.0$ mm in the isotropic phase. On LCITS, we measure $L = 0.1 \pm 0.1$ mm in the nematic phase and $L = 0.2 \pm 0.1$ mm in the isotropic phase. These results are consistent with the expectation that a higher lubricant surface tension leads to a slightly more extended wetting ridge, which aligns with our observation that wetting ridges extend farther horizontally in the isotropic phase where the LC surface tension is higher.[14] Although LCs are intrinsically anisotropic, 5CB and 8CB behave as Newtonian fluids in both nematic and isotropic phases, with shear-rate independent apparent viscosity.[55,56] Consistent with prior studies,[14,27,32,36,57] we observe no unusual wetting ridge formation or dynamics on LC-infused surfaces compared to oil-infused surfaces. More generally, wetting ridges on silicone oil-infused surfaces and on liquid crystal-infused surfaces are comparable in size, because their steady-state geometry depends primarily on lubricant availability, rather than on differences in the rheological nature of the infused liquid.[14,57]

4.1 Capillary-assisted droplet attraction (stage I)

To initiate coalescence, we moved one droplet towards the other so that the wetting ridges just overlapped, which triggered the attraction (Fig. 2f). The measured u_1 values for LCITS and LCIPS, together with the theoretical u_1 values based on the model, are summarized in Table 2.

On LCITS, the measured values of u_1 agree with the theoretical predictions in both phases, although the measurement uncertainty is relatively high. All uncertainties reported in this

Table 2 Measured (u_1^{exp}) and theoretical (u_1) values of the first peak velocity for droplet approach on LCITS and LCIPS at different temperatures (T), corresponding to the nematic and isotropic phases of 5CB and 8CB. Theoretical values are calculated from eqn (2) for comparison with the experiment. Errors represent one standard deviation from the mean, based on 10 repeated measurements for each table entry

Surface	T [°C]	u_1^{exp} [mm s^{-1}]	u_1 [mm s^{-1}]
LCITS	30	13 ± 7	≈16
LCITS	40	26 ± 20	≈42
LCIPS	40	2 ± 2	≈17
LCIPS	50	3 ± 1	≈36

work correspond to one standard deviation from the mean of multiple measurements. In contrast, the measured values of u_1 on LCIPS deviate significantly from theory. The measured u_1 values thus appear independent of the LC phase, as they are equal within experimental uncertainty in both cases and are approximately an order of magnitude lower than the model predicts. In all cases, droplets are pulled towards each other by an attractive capillary force balanced by viscous resistance. For a single droplet sliding on a smooth lubricant-infused surface, it was recently shown that the friction force decreases as the thickness of the lubricant layer increases and eventually plateaus above 100 μm.[59] Conversely, previous work on coalescing droplets on oil-infused SLIPS reports that the approach speed decreases as the ratio h_{wr}/R increases,[36] where h_{wr} is the height of the wetting ridge and R is the droplet radius. This ratio provides a relative measure of the volume of lubricant that resists motion, and h_{wr} itself depends on the availability of the lubricant, *i.e.* on the lubricant film thickness.[57] Consistent with this, the wetting ridge heights observed on LCIPS were almost three times greater than on LCITS ($h_{wr}/R = 0.6 ± 0.1 > 0.24 ± 0.08$), and the associated u_1 values were much lower (Table 2). These results suggest that, for long-range droplet–droplet interactions, the increase in resistance to motion associated with wetting ridge growth from a thicker lubricant film dominates over the reduction in single-droplet friction that occurs with increasing film thickness. Furthermore, because the attractive capillary force scales as $F_\gamma \sim \gamma l R$ and depends primarily on the droplet radius and lubricant surface tension, two droplets of equal size experience comparable driving forces. Consequently, differences in approach velocity arise primarily from differences in the effective mass that must be accelerated. In systems with a larger wetting ridge volume, a greater fraction of the capillary force is expended accelerating the droplets, resulting in slower motion. This interpretation is consistent with our observation; droplets on LCIPS exhibit lower approach velocities due to the larger effective mass associated with the wetting ridge.

Next, we measured u_h, which has previously been shown to be approximately equal in magnitude to the horizontal approach velocity of the droplets.[36] To estimate u_h, we calculated an average velocity from the change in meniscus height over several frames. Because the change in meniscus height was determined manually from discrete images rather than tracked continuously in each frame, the measured velocities

represent temporal averages rather than instantaneous values and therefore underestimate the true peak velocities. Moreover, because the velocity on LCITS is substantially higher than on LCIPS, the manual height determination carries greater uncertainty in the LCITS case, resulting in a larger spread in the data, whereas the slower dynamics on LCIPS yield more consistent measurements. Despite the scatter in the data, we observe a clear positive linear trend between u_1 and u_h across both LCITS and LCIPS. This is quantified by a Pearson correlation coefficient of approximately 0.8 and a Spearman rank correlation coefficient of approximately 0.9, indicating a strong approximately linear and monotonic relationship between u_1 and u_h (Fig. 4a). Taken together, these statistics support the conclusion that u_1 and u_h scale approximately linearly with one another, despite our systematic underestimation of u_h. This behavior is also consistent with the theoretical framework presented in Section 3, which predicts that the droplet approach and meniscus rise velocities are comparable in magnitude and peak values, independent of surface type, following strictly from geometrical considerations – a relationship previously confirmed experimentally on oil-infused SLIPS. In a previous study,[36] oscillations in l with a timescale of 20 ms were observed in the first stage of coalescence on oil-infused SLIPS. In our experiments, no such oscillations at the first peak were detected on LCITS or LCIPS (Fig. 3d). We attribute this to noise and limited temporal resolution in our numerical analysis, which reduce the precision of $l(t)$ and therefore prevent us from definitively ruling out the presence of small-amplitude oscillations on these surfaces. However, it is also plausible that the post-merge response is critically or overdamped, which would suppress resolvable oscillations. In particular, the substantially larger wetting ridges on LCIPS are expected to increase both the effective inertia and the dissipative resistance through ridge deformation and viscous flow in the confined lubricant film. This combination shifts the dynamics towards stronger damping and can eliminate oscillations at the first velocity peak within our temporal resolution. Moreover, any oscillatory motion would further deform the wetting ridge and confined film, increasing dissipation and favoring rapid relaxation.

4.2 Wetting ridge lubricant drainage (stage II)

After the droplets collide, the LC film trapped between them drains radially outward until it reaches a critical thickness and collapses, resulting in droplet merging. The measured drainage times are presented in Table 3. Because the viscosity of 5CB and 8CB differs only slightly between the nematic and isotropic phases, we report the results here primarily as a function of droplet radius.

On LCIPS, we observed longer drainage times for smaller droplets, in contrast to the theoretical model, which predicts shorter drainage times for droplets with smaller radii. On LCITS, the drainage times showed no clear dependence on droplet radius. We attribute the discrepancy between measurements and theory primarily to an underestimation of the drainage times for larger droplets. Larger droplets collide at higher Weber numbers (We = $\rho R u_1^2/\gamma$), which can
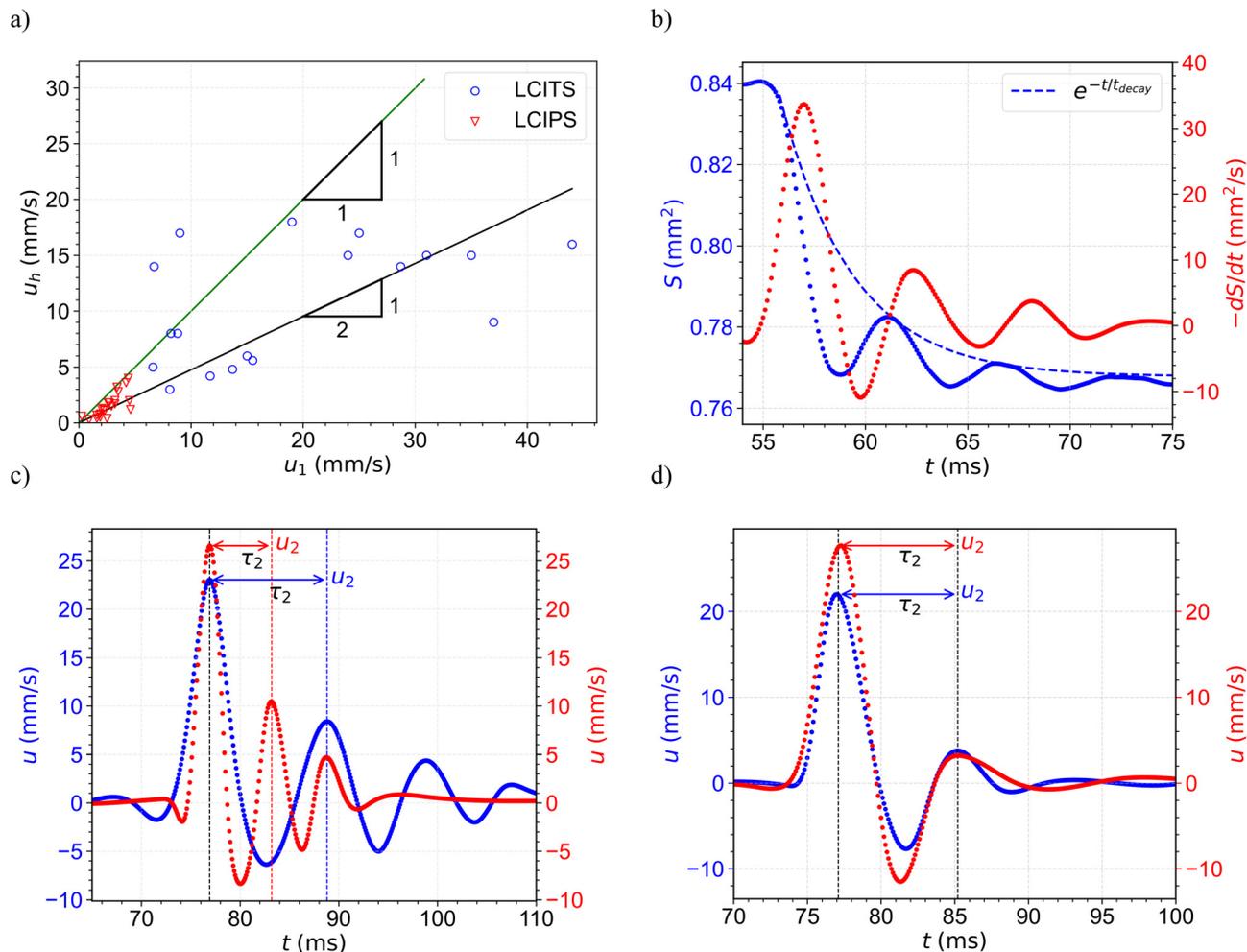
Fig. 4 (a) Comparison of the first peak droplet approach velocity (u_1) and peak meniscus rise velocity (u_h) measured on LCITS and LCIPS. The solid black line represents a linear fit obtained from the combined LCITS and LCIPS datasets, justified by the geometric origin of the expected relationship. Ordinary least-squares fit constrained through the origin yields $u_h = au_1$ with $a = 0.476 \pm 0.039$. The solid green line denotes the 1:1 relationship $u_h = u_1$, corresponding to the case in which the two velocities are exactly equal. The larger data spread observed for LCITS reflects greater measurement uncertainty associated with the manual determination of meniscus displacement from discrete images; the faster dynamics on LCITS increase this uncertainty, while the slower velocities on LCIPS yield more consistent measurements. The strong correlation between u_1 and u_h confirms the theoretical prediction that their magnitudes are approximately equal. (b) Time evolution of the total droplet cross-sectional area ((S), left axis) and its time derivative (($-dS/dt$), right axis) during the merging of two droplets. Both S and its time derivative show exponential decay. Fitting an exponential decay envelope to the data yields the characteristic decay time (t_{decay}). Instantaneous velocity of coalescing droplets: (c) two droplets with different radii $R \approx 0.5$ mm (left axis) and $R \approx 0.4$ mm (right axis), on LCITS in the nematic phase; and (d) two droplets with equal radius ($R \approx 0.3$ mm) on LCIPS in the nematic (left axis) and isotropic (right axis) phases. On LCITS, the smaller droplet exhibited a higher peak velocity and a shorter oscillation period than the larger droplet. On LCIPS, droplets on the isotropic phase reached higher peak velocities than on the nematic phase, while the oscillation period at the second peak (τ_2) remained approximately equal.

Table 3 Measured (Δt_{exp}) and theoretical (Δt) drainage times of droplets on LCITS and LCIPS as a function of droplet radius R. Errors represent one standard deviation from the mean, based on 5 repeated measurements for each entry

Surface	R [mm]	Δt_{exp} [s]	Δt [s]
LCITS	0.4 ± 0.1	13 ± 7	31 ± 12
LCITS	0.5 ± 0.1	13 ± 5	41 ± 8
LCIPS	0.3 ± 0.1	26 ± 8	30 ± 3
LCIPS	0.5 ± 0.1	16 ± 4	52 ± 24

produce a thinner lubricant film after collision and thus shorten drainage times.[13] Because the surfaces were heated to maintain the desired LC phases, water droplets evaporated more rapidly. To limit evaporation-induced changes in droplet radius, we excluded cases in which merging did not occur within approximately 60 s. Larger droplets exhibit greater variability in drainage times due to their higher Weber numbers, so this filtering biases the measurements towards shorter drainage times for larger droplets. This bias likely contributes to the apparent discrepancy with theoretical predictions.

4.3 Droplet merging (stage III)

After the thin film separating the droplets collapses, the droplets merge into a single larger droplet (Fig. 3a and b) and their total surface area decreases (Fig. 4b). The surface free energy released during merging is partially converted into in-plane translational kinetic energy because the wetting ridge prevents the droplet from jumping. This release of surface free energy manifests as the second peak in the velocity u_2. The measured values of u_2 on LCITS and LCIPS are shown in Table 4.

On both LCITS and LCIPS, the measured u_2 values were approximately an order of magnitude lower than the theoretical predictions, which assume full conversion of the released surface free energy into translational kinetic energy. In our experiments, only about 8% of the available surface free energy was converted into translational motion. On LCITS, u_2 followed the model trend: smaller droplets reached higher velocities than larger ones (Fig. 4d). However, u_2 showed no clear dependence on the LC phase. On LCIPS, u_2 appeared independent of droplet size and instead varied primarily with the LC phase, remaining approximately constant for different radii within each phase (Fig. 4c). Moreover, the measured values of u_2 on LCIPS were slightly lower than those on LCITS. We attribute these lower velocities on LCIPS to the larger volume of LC in the wetting ridge, which increases resistance to motion. This interpretation is consistent with the damped harmonic oscillator model of droplet coalescence, where a larger wetting ridge volume adds effective mass and reduces the peak velocity following energy release. Accordingly, longer oscillation periods and decay times are expected, as observed here. The apparent independence of u_2 on droplet size on LCIPS may indicate that the wetting ridge volume exceeds a threshold beyond which u_2 is governed by the wetting ridge morphology and mass distribution rather than by the droplet radius alone. In this regime, variations in R likely compete with phase-dependent changes in wetting ridge size, leading to an apparent insensitivity of u_2 to R within each phase.

For LCITS, we determined the scaling of the second peak velocity with droplet radius. The measured scaling exponents were -0.5 ± 0.8 for the nematic phase and -1.4 ± 1.8 for the

isotropic phase. These values are consistent with the theoretical scaling exponent of $-1/2$ within experimental uncertainty. For the nematic case, the result supports the model; for the isotropic case, the data are compatible with the model within uncertainty but are not precise enough to provide a stringent test.

After merging, the resulting droplet oscillates in the horizontal direction. This motion can be modelled as an underdamped mass–spring harmonic oscillator, which we verified by tracking the total cross-sectional area $S(t)$ and its derivative $-dS/dt$, both of which oscillate with period τ_2 and decay with an exponential envelope of the form $\exp(-t/t_{\mathrm{decay}})$ (Fig. 4b). The measured values of τ_2 are presented in Table 5. Although the measured values of τ_2 are approximately an order of magnitude larger than the theoretical predictions, they follow the trends predicted by the model, particularly the scaling with droplet radius, where smaller droplets exhibit shorter oscillation periods (Fig. 4c). No significant differences in τ_2 were observed between mesophases for droplets of similar size on either substrate (Fig. 4d). This is consistent with eqn (7), which depends primarily on the droplet radius and is independent of viscosity. τ_2 was also slightly longer on LCIPS, consistent with the additional effective mass of the wetting ridge; this contribution is not included in the original model and may explain why the measured values exceed the theoretical predictions.

Next, we determined the scaling exponent of τ_2 with the radius of the droplet. On LCITS, the exponents were 1.5 ± 1.3 for the nematic phase and 2.3 ± 3.6 for the isotropic phase, while on LCIPS they were 0.5 ± 0.3 for the nematic phase and 0.7 ± 0.7 for the isotropic phase. On LCITS, the measured scaling exponent for the nematic phase is consistent, within experimental uncertainty, with the theoretical scaling $\tau_2 \sim (\rho R^3/\gamma_{\mathrm{eff}})^{1/2}$. For the isotropic phase, the measured exponent deviates more strongly from theory, with the large uncertainty arising from cumulative error propagation. In contrast, on LCIPS, the measured scaling exponents were closer to $1/2$ than to the theoretical $3/2$. This behavior is consistent with a larger wetting ridge that increases the effective mass of the droplet,

Table 4 Measured (u_2^{exp}) and theoretical (u_2) values of the second velocity peak on LCITS and LCIPS at different temperatures T and droplet radii R. Errors represent one standard deviation from the mean, based on 5 repeated measurements for each entry

T [°C]	R [mm]	u_2^{exp} [mm s^{-1}]	u_2 [mm s^{-1}]
LCITS			
30	0.4 ± 0.1	36 ± 7	≈ 410
30	0.6 ± 0.1	29 ± 7	≈ 350
40	0.5 ± 0.1	44 ± 5	≈ 440
40	0.6 ± 0.1	30 ± 10	≈ 400
LCIPS			
40	0.3 ± 0.1	23 ± 7	≈ 410
40	0.7 ± 0.2	21 ± 5	≈ 280
50	0.4 ± 0.2	30 ± 6	≈ 370
50	0.8 ± 0.2	30 ± 10	≈ 270

Table 5 Measured (τ_2^{exp}) and theoretical (τ_2) values of the oscillation period, as well as measured characteristic decay times (t_{decay}) at the second peak on LCITS and LCIPS at different temperatures T and droplet radii R. Errors represent one standard deviation from the mean, based on 5 repeated measurements for each entry

T [°C]	R [mm]	τ_2^{exp} [ms]	τ_2 [ms]	t_{decay} [ms]
LCITS				
30	0.4 ± 0.1	6 ± 1	≈ 1.1	5 ± 2
40	0.5 ± 0.1	7 ± 1	≈ 1.2	4 ± 1
30	0.6 ± 0.1	11 ± 1	≈ 1.8	11 ± 4
40	0.6 ± 0.2	11 ± 1	≈ 1.6	7 ± 1
LCIPS				
40	0.3 ± 0.1	8 ± 1	≈ 0.8	6 ± 1
50	0.4 ± 0.2	8 ± 1	≈ 1.2	5 ± 1
40	0.6 ± 0.2	13 ± 3	≈ 2.6	$14 \pm$
50	0.8 ± 0.2	14 ± 3	≈ 3.2	13 ± 5

thereby lengthening the oscillation period and shifting the scaling exponent from the droplet-only prediction.

To determine characteristic decay times, we fitted an exponential decay envelope of the form $\exp(-t/t_{\text{decay}})$ to $-dS/dt$; the resulting values are listed in Table 5. The characteristic decay times show only a weak dependence on phase, consistent with the small difference in viscosity between the nematic and isotropic phases of either LC, compared to the quadratic scaling of the characteristic decay time with droplet radius ($t_{\text{decay}} \sim R^2/\eta_{\text{LC}}$).[36] Decay times were slightly longer on LCIPS than on LCITS, consistent with a larger wetting ridge volume that increases the effective mass in the underdamped harmonic oscillator model and thereby lengthens the decay time. Based on our measurements, the characteristic decay times scale approximately quadratically with droplet radius on both surfaces and for both mesophases. On LCITS, the measured exponent was 2.0 ± 2.0 for the nematic phase and 1.8 ± 1.7 for the isotropic phase, while on LCIPS the measured exponent was 1.8 ± 0.7 for the nematic phase and 1.8 ± 1.5 for the isotropic phase. These results are consistent, within the experimental uncertainty, with the theoretical scaling $t_{\text{decay}} \sim R^2$, confirming the quadratic dependence of the decay time on droplet radius.

5. Conclusions

In this study, we experimentally investigated the attraction and coalescence of millimeter-sized water droplets on LCITS and LCIPS, and compared the observations with the theoretical framework of Xu *et al.*[36] In both systems, coalescence proceeds through the same qualitative sequence – droplet attraction, LC drainage, film rupture and merging, followed by post-coalescence oscillations – as previously reported for oil-infused SLIPS. Quantitatively, however, LCIPS exhibits systematic deviations from the theory.

During the initial attraction stage, peak approach velocities on LCITS agree with theoretical predictions, whereas on LCIPS they are strongly suppressed and largely independent of the LC phase. This suppression is consistent with the substantially larger wetting ridges on LCIPS, which increase hydrodynamic resistance and effective inertia. In the second stage, the characteristic drainage times remain of the same order of magnitude as predicted. The apparent inversion of the size dependence (smaller droplets exhibiting longer drainage times) is attributed to an experimental bias: larger droplets display greater variability in drainage times, and evaporation-driven constraints preferentially remove longer drainage events for larger droplets, biasing the measured trend. After merging, the second velocity peak is smaller than predicted on both surfaces, indicating that only a fraction of the available surface free energy is converted into translational kinetic energy. On LCITS, the peak velocity dependence on droplet size follows theoretical expectations, whereas on LCIPS it is governed primarily by the LC phase and is systematically reduced. Despite this additional damping, in-plane oscillations persist on both surfaces.

The oscillation periods and decay times scale primarily with droplet size but exceed theoretical predictions, highlighting the role of wetting-ridge inertia and enhanced dissipation. Taken together, these results delineate the regime of applicability of the Xu *et al.* framework and emphasize that wetting-ridge geometry – and, potentially, LC-specific rheology – must be incorporated to describe coalescence on LC-infused surfaces with large ridges.

More broadly, LCITS and LCIPS provide SLIPS-like coalescence dynamics while offering additional control parameters, including LC phase, lubricant thickness, and substrate architecture, which collectively tune droplet mobility and droplet–droplet interactions. While the present study focuses on electrolyte-free droplets, ion-specific effects at LC–aqueous interfaces are known to induce interfacial ordering at sufficiently high salt concentrations. Future work will therefore examine how electrolyte identity and concentration modulate LC anchoring, interfacial ordering, and coalescence dynamics. In parallel, extending the experiments to evaporation-dominated conditions and developing refined models that explicitly include wetting-ridge mass and LC-specific dissipation will be important steps towards predicting lubricant depletion and optimizing cargo transport on stimuli-responsive LC-infused surfaces.

Conflicts of interest

There are no conflicts to declare.

Data availability

All data generated or analysed during this study are included in this published article [and its supplementary information files]. The supplementary information contains additional methodological details (white light interferometry and spin-coating) as well as additional parameters used in calculations along with four supplementary movies. Supplementary information is available. See DOI: https://doi.org/10.1039/d5sm01184a.

Acknowledgements

References

1 J. Genzer and K. Efimenko, *Biofouling*, 2006, **22**, 339–360.
2 U. Manna, N. Raman, M. A. Welsh, Y. M. Zayas-Gonzalez, H. E. Blackwell, S. P. Palecek and D. M. Lynn, *Adv. Funct. Mater.*, 2016, **26**, 3599–3611.

3 M. J. Kratochvil, M. A. Welsh, U. Manna, B. J. Ortiz, H. E. Blackwell and D. M. Lynn, *ACS Infect. Dis.*, 2016, **2**, 509–517.

4 P. Kim, T.-S. Wong, J. Alvarenga, M. J. Kreder, W. E. Adorno-Martinez and J. Aizenberg, *ACS Nano*, 2012, **6**, 6569–6577.

5 H. Liu, P. Zhang, M. Liu, S. Wang and L. Jiang, *Adv. Mater.*, 2013, **25**, 4477–4481.

6 T.-S. Wong, S. H. Kang, S. K. Y. Tang, E. J. Smythe, B. D. Hatto, A. Grinthal and J. Aizenberg, *Nature*, 2011, **477**, 443–447.

7 A. Lafuma and D. Quere, *Europhys. Lett.*, 2011, **96**, 56001.

8 D. Daniel, J. V. I. Timonen, R. Li, S. J. Velling, M. J. Kreder, A. Tetreault and J. Aizenberg, *Phys. Rev. Lett.*, 2018, **120**, 244503.

9 A. Keiser, L. Keiser, C. Clanet and D. Quere, *Soft Matter*, 2017, **13**, 6981–6987.

10 D. Daniel, J. V. I. Timonen, R. Li, S. J. Velling and J. Aizenberg, *Nat. Phys.*, 2017, **13**, 1020–1025.

11 M. J. Kreder, D. Daniel, A. Tetreault, Z. Cao, B. Lemaire, J. V. I. Timonen and J. Aizenberg, *Phys. Rev. X*, 2018, **8**, 031053.

12 F. Schellenberger, J. Xie, N. Encinas, A. Hardy, M. Klapper, P. Papadopoulos, H.-J. Butt and D. Vollmer, *Soft Matter*, 2015, **11**, 7617–7626.

13 J. B. Boreyko, G. Polizos, P. G. Datskos, S. A. Sarles and C. P. Collier, *Proc. Natl. Acad. Sci. U. S. A.*, 2014, **111**, 7588–7593.

14 M. Tress, S. Karpitschka, P. Papadopoulos, J. H. Snoeijer, D. Vollmer and H.-J. Butt, *Soft Matter*, 2017, **13**, 3760–3767.

15 S. Adera, J. Alvarenga, A. V. Shneidman, C. T. Zhang, A. Davitt and J. Aizenberg, *ACS Nano*, 2020, **14**, 8024–8035.

16 D. P. Regan and C. Howell, *Curr. Opin. Colloid Interface Sci.*, 2019, **39**, 137–147.

17 J. Ahn, J. Jeon, C. S. Heu and D. R. Kim, *Adv. Mater. Interfaces*, 2018, **5**, 1800980.

18 Y. Zheng, J. Cheng, C. Zhou, H. Xing, X. Wen, P. Pi and S. Xu, *Langmuir*, 2017, **33**, 4172–4177.

19 C. Liu, H. Ding, Z. Wu, B. Gao, F. Fu, L. Shang, Z. Gu and Y. Zhao, *Adv. Funct. Mater.*, 2016, **26**, 7937–7942.

20 J. Jiang, J. Gao, H. Zhang, W. He, J. Zhang, D. Daniel and X. Yao, *Proc. Natl. Acad. Sci. U. S. A.*, 2019, **116**, 2482–2487.

21 E. Bukusoglu, M. Bedolla Pantoja, P. C. Mushenheim, X. Wang and N. L. Abbott, *Annu. Rev. Chem. Biomol. Eng.*, 2016, **7**, 163–196.

22 T. Emeršič, R. Zhang, Ž. Kos, S. Čopar, N. Osterman, J. J. de Pablo and U. Tkalec, *Sci. Adv.*, 2019, **5**, eaav4283.

23 S. Čopar, Ž. Kos, T. Emeršič and U. Tkalec, *Nat. Commun.*, 2020, **11**, 59.

24 I. Kim, M. A. Ansari, M. Q. Mehmood, W.-S. Kim, J. Jang, M. Zubair, Y.-K. Kim and J. Rho, *Adv. Mater.*, 2020, **32**, 2004664.

25 A. M. Rather, Y. Xu, Y. Chang, R. L. Dupont, A. Borbora, U. I. Kara, J.-C. Fang, R. Mamtani, M. Zhang, Y. Yao, S. Adera, X. Bao, U. Manna and X. Wang, *Adv. Mater.*, 2022, **34**, 2110085.

26 Y. Xu, Y. Chang, Y. Yao, M. Zhang, R. L. Dupont, A. M. Rather, X. Bao and X. Wang, *Adv. Mater.*, 2022, **34**, 2108788.

27 Y. Xu, Y. Yao, W. Deng, J.-C. Fang, R. L. Dupont, M. Zhang, S. Čopar, U. Tkalec and X. Wang, *Nano Res.*, 2023, **16**, 5098–5107.

28 A. Borbora, Y. Xu, S. Dey, X. Wang, Y. Yao, B. B. Mandal, X. Wang and U. Manna, *Adv. Mater.*, 2023, **35**, 2302264.

29 D. H. Chang, F. Wang, S. P. Palecek and D. M. Lynn, *ACS Appl. Mater. Interfaces*, 2025, **17**, 27882–27894.

30 U. I. Kara, B. Chen, S. Čopar, S. Li, R. Mamtani, Y. Xu, A. H. Weible, E. C. Boerner, Z. Yang, Y. Yao, R. L. B. Selinger, U. Tkalec and X. Wang, *Nat. Phys.*, 2025, **21**, 1404–1411.

31 H. Agarwal, K. E. Nyffeler, U. Manna, H. E. Blackwell and D. M. Lynn, *ACS Appl. Mater. Interfaces*, 2021, **13**, 33652–33663.

32 Y. Xu, A. M. Rather, Y. Yao, J.-C. Fang, R. S. Mamtani, R. K. A. Bennett, R. G. Atta, S. Adera, U. Tkalec and X. Wang, *Sci. Adv.*, 2021, **7**, eabi7607.

33 J. D. Smith, R. Dhiman, S. Anand, E. Reza-Garduno, R. E. Cohen, G. H. McKinley and K. K. Varanasi, *Soft Matter*, 2013, **9**, 1772–1780.

34 H. Xu, J. M. Herzog, Y. Zhou, Y. Bashirzadeh, A. Liu and S. Adera, *ACS Nano*, 2024, **18**, 4068–4076.

35 J. Sun and P. B. Weisensee, *Soft Matter*, 2019, **15**, 4808–4817.

36 H. Xu, Y. Zhou, D. Daniel, J. Herzog, X. Wang, V. Sick and S. Adera, *Nat. Commun.*, 2023, **14**, 4901.

37 M. Lin, P. Kim, S. Arunachalam, R. Hardian, S. Adera, J. Aizenberg, X. Yao and D. Daniel, *Phys. Rev. Lett.*, 2024, **132**, 058203.

38 J. H. Guan, G. G. Wells, B. Xu, G. McHale, D. Wood, J. Martin and S. Stuart-Cole, *Langmuir*, 2015, **31**, 11781–11789.

39 A. Keiser, P. Baumli, D. Vollmer and D. Quéré, *Phys. Rev. Fluids*, 2020, **5**, 014005.

40 L. Hauer, A. Naga, R. G. M. Badr, J. T. Pham, W. S. Y. Wong and D. Vollmer, *Soft Matter*, 2024, **20**, 5273–5295.

41 M. S. Sadullah, C. Semprebon and H. Kusumaatmaja, *Langmuir*, 2018, **34**, 8112–8118.

42 R. Roy, R. L. Seiler, J. A. Weibel and S. V. Garimella, *Adv. Mater. Interfaces*, 2020, **7**, 2000731.

43 J. Eggers, J. R. Lister and H. A. Stone, *J. Fluid Mech.*, 1999, **401**, 293–310.

44 D. G. A. L. Aarts, H. N. W. Lekkerkerker, H. Guo, G. H. Wegdam and D. Bonn, *Phys. Rev. Lett.*, 2005, **95**, 164503.

45 S. Hardt and G. McHale, *Annu. Rev. Fluid Mech.*, 2022, **54**, 83–104.

46 J. Lim, G. Lee, B. Kim, S. Y. Lee, S. Yoon, S. Hong, J. Oh and W. C. Lee, *ACS Appl. Mater. Interfaces*, 2025, **17**, 34418–34432.

47 D. A. Dunmur, M. R. Manterfield, W. H. Miller and J. K. Dunleavy, *Mol. Cryst. Liq. Cryst.*, 1978, **45**, 127–144.

48 M. Sandmann, F. Hamann and A. Wurflinger, *Z. Naturforsch. A*, 1997, **52**, 739–747.

49 M. Sandmann and A. Wurflinger, *Z. Naturforsch. A*, 1998, **53**, 787–792.

50 A. G. Chmielewski, *Mol. Cryst. Liq. Cryst.*, 1986, **132**, 339–352.

51 M. G. J. Gannon and T. E. Faber, *Philos. Mag. A*, 1978, **37**, 117–135.

52 L. W. Honaker, A. Sharma, A. Schanen and J. P. F. Lagerwall, *Crystals*, 2021, **11**, 687.

53 Z. Wang, Q. Xu, L. Wang, L. Heng and L. Jiang, *J. Mater. Chem. A*, 2019, **7**, 18510–18518.

54 H. Kneppe, F. Schneider and N. K. Sharma, *Ber. Bunsen-Ges. Phys. Chem.*, 1981, **85**, 784–789.

55 K. Mukai, F. Kishi and T. Amari, *Nihon Reoroji Gakkaishi*, 1997, **25**, 155–160.

56 D. Porter, J. R. Savage, I. Cohen, P. Spicer and M. Caggioni, *Phys. Rev. E: Stat., Nonlinear, Soft Matter Phys.*, 2012, **85**, 041701.

57 H. Xu, T. Kulakowski, Y. J. Lee and S. Adera, *ACS Appl. Mater. Interfaces*, 2025, **17**, 31677–31684.

58 W. M. Schwartz and H. W. Moseley, *J. Phys. Colloid Chem.*, 1947, **51**, 826–837.

59 R. Sakai, T. Hiroi, R. Tamate, T. Mouterde and M. Tenjimbayashi, *Appl. Phys. Lett.*, 2025, **126**, 231602.